Geoderma 435 (2023) 116497

Contents lists available at ScienceDirect

Geoderma

journal homepage: www.elsevier.com/locate/geoderma

Continuum and discrete element modelling for describing coupled hydro-mechanical effects of earthworm burrow coatings on soil shrinkage

Luis Alfredo Pires Barbosa *, Horst H. Gerke

Research Area 1 "Landscape Functioning". Leibniz Centre for Agricultural Landscape Research (ZALF), Müncheberg, Germany

ARTICLE INFO

Handling Editor: Yvan Capowiez

Keywords:
Earthworm burrow
Organo-mineral coating
Mass exchange
Drying soil
Capillary stress
Soil pore network dynamics

ABSTRACT

Structured soils with earthworm burrows are locally heterogeneous due to coatings along these biopore walls that are superimposed on the inter- and intra-aggregate pore network of the soil matrix. The partially compacted finer-textured and organic matter-rich coatings can limit the flow exchange between the macropores and the soil matrix during preferential flow. Still unknown are dynamic hydro-mechanical interrelations in coating and matrix domains that affect stress–strain behaviour at the macroscopic scale. Such hydro-mechanic interactions may be described with the discrete element method (DEM) coupled with a two-phase pore finite volume (2PFV) approach if relevant pore structures are represented in the model. The objective was to develop a coupled DEM-2PFV model together with a parameterization procedure. Major task was to create a parameterization procedure to calibrate micro parameters of the model by macro properties quantified from drainage experiments of soil samples with earthworm burrow wall coatings.

The solid phase was modelled by particle aggregation creating inter and intra-aggregate pore network for the soil matrix in a cube of about 5 cm edge length and one side with the coating structure. This DEM model was coupled with a 2PFV model to simulate hydro-mechanic effects during drainage. Sand box drainage experiments were carried out on soil matrix and biopore samples with laser surface elevation measurements to obtain the mechanical stress–strain macro parameters necessary for model calibration. The poly-dispersed DEM-2PFV model was able to describe effects of two-phase air–water flow on stress–strain macro parameters. The micro parameters (i.e., particle stiffness and bond strength) of the pore scale model were obtained from macro parameters of the primary and secondary stress–strain stages by training a random forest *meta*-estimator. The model was able to reproduce the pore network of coating material and the inter- and intra-aggregate pore network of the matrix that are dynamically changing with the effective stress. The machine learning model revealed that the bond strength among particles within aggregates governed the shrinkage of soil matrix, while the particle stiffness of the coating material reduced the susceptibility of aggregate breakage producing a more stable inter-aggregated pore network during the drainage process. This study confirmed that coating material present in biopore surface increases the horizontal soil hydro structural stability. The microscale hydro-mechanic modelling can be useful for finding flow exchange parameters inputs for upscaled models and correlating pore-scale parameters to experimentally determined stress–strain macro parameters.

1. Introduction

Flow exchange between the macropore surface and the soil matrix is one of the key processes controlling preferential flow and local non-equilibrium conditions in structured soils (Jarvis, 2007). Preferential pathways (i.e. macropores) may be formed as a result of biotic (e.g. earthworm burrows, decayed root channels) or abiotic processes that cause soil fragmentation (i.e., the network of inter-aggregate pores and desiccation cracks). The extent to which water infiltration bypasses the soil matrix brings benefits and risks affecting root zone drainage, plant nutrient transport (Morales et al., 2010), and the filtering function of soil by potentially increasing leaching of chemicals to groundwater (Köhne et al., 2009; Shipitalo et al., 2000).

Continuum scale numerical models describing non-equilibrium type of preferential flow are mainly based on the two-domain dual-permeability approach (c.f. Gerke, 2006), and pore-scale flow in macropore networks based on X-ray CT images (e.g. Köhne et al., 2011) was coupled with continuum-scale flow in the matrix domain. However,

* Corresponding author.
E-mail address: luis.pires@zalf.de (L.A.P. Barbosa).

https://doi.org/10.1016/j.geoderma.2023.116497
Received 15 December 2022; Received in revised form 24 April 2023; Accepted 1 May 2023

none of these models have yet tried to incorporate the required properties (e.g. distribution of organic cementing agents and wettability) that reproduce the heterogeneity of the system's smaller-scale soil pores, nor the structural dynamics of the soil (Vereecken et al., 2016).

Soil biopores such as earthworm burrows and decayed root channels that serve as preferential flow paths overlap with the inter- and intra-aggregate pore network in structured soils (e.g. Jarvis, 2007; Vogel et al., 2022) (drilosphere scale Fig. 1). The biopores have been identified as biological "hot spots" (Bundt et al., 2001) because of an increased microbial biomass, organic carbon and enzyme activity along macropore surfaces (Leue et al., 2021). Organo-mineral associations from worm casts and mucus as well as root exudates are present in biopore wall coatings (Capowiez et al., 2021). This microbial activity increases the local production of a biofilm and the formation of organo-mineral associations, which both is increasing cementing forces of the soil particles in the wall surrounding the earthworm burrow (Czarnes et al., 2000; Peng et al., 2011) and locally reducing the wettability (e.g., Ellerbrock and Gerke, 2013). In addition to the production and deposition of exudates (Becker and Holz, 2021), the activity of roots or earthworms may also compact the surrounding soil matrix (Badorreck et al., 2012; Lucas et al., 2019; Ruiz et al., 2015) forming some kind of an interface between biopores and the soil matrix.

The combination of all the above described properties and processes forming the biopore coating material may control flow exchange between the macropore surface and the soil matrix during preferential flow events and drying processes (Fig. 1), however little is known about the effects of biopore coating material on hydro-mechanical dynamics of mass exchange processes (Haas et al., 2020). Gerke and Köhne (2002) found that the coating hydraulic conductivity function was considerably reduced in the near saturation range. However, neither soil mechanical properties nor soil structural dynamics were considered yet. Simulations (Barbosa et al., 2022a) showed that higher binding forces among particles in the coating material increase the stiffness, suggesting higher mechanical stability of the biopore structure (Schäffer et al., 2008a). This affects the dynamics of secondary pore system network formation (van der Linden et al., 2019), which links the biopore surface with the soil matrix (Le Mer et al., 2021) since stronger cementing forces between particles modify the formation of desiccation cracks (Tang et al., 2021) (Fig. 1). Therefore, the cracking induced changes of the permeability between coated biopore and matrix pore region (c.f. Barbosa et al., 2022a) can dynamically affect macropore-matrix mass exchange rate coefficients (Fig. 1) (Gerke and van Genuchten, 1996) that are currently assumed to be constant (e.g. Faúndez Urbina et al., 2021).

The discrete element method (DEM) has been proposed (Cundall and Strack, 1979) for modelling elasto-plastic deformations as well as fragmentation of granular material (Barbosa, 2020; Barbosa et al., 2020). Barbosa et al. (2022b) developed a Weibull distribution approach for DEM, to model the effect of coating distribution heterogeneity on mechanical properties of different soil aggregate shapes and established a relationship between coating heterogeneity and crack surface area generated after aggregate tensile failure. Using DEM, Bentz et al. (2022) investigated the influence of spatially heterogeneous wettability distributions on infiltration into porous media by assuming a distribution of contact angles in the porous medium for a simplified geometry.

Mesh-based approaches (e.g., pore finite volume method and Lattice Boltzmann Method) are frequently used to solve variations of Navier-Stokes equations on the pore scale (Meakin and Tartakovsky, 2009). Despite their proven accuracy, mesh-based approaches have difficulties to simulate free surface flows (e.g., non-saturated flow along macropore walls) and moving geometries (i.e., dynamic change of soil structure) due to their dependency on the mesh topology. This increases computational effort due to costly adaptive of re-meshing algorithms, imposing a limitation for upscaling simulations (Dal Ferro et al., 2015).

Hence, coupling different numerical approaches to solve the mechanical complexity of granular and discontinuous materials with fluid dynamics methods can shed light on the dynamic interaction between soil deformation, crack formation and propagation, and hydraulic properties at pore scale level (Fig. 1) (Tang et al., 2021). Recently, a three dimensional (3D) numerical coupling DEM and Pore Finite Volume (PFV), a class of pore network models, was introduced to simulate complex hydro-mechanical interactions (Yuan et al., 2016). Yuan and Chareyre (2017) added hydro-mechanical responses in DEM simulations

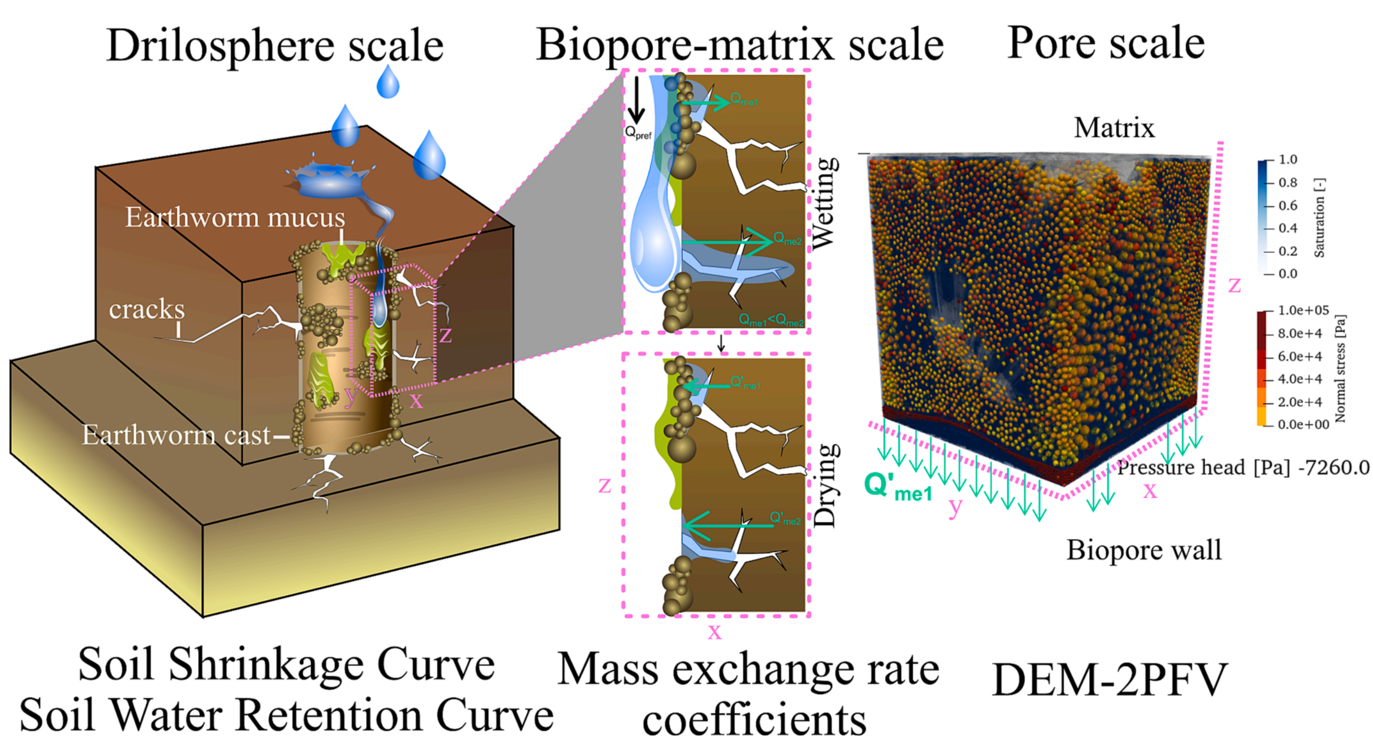

Fig. 1. Linking micro parameters of the hydro-mechanical pore scale numerical modelling (DEM-2PFV) (right) with mass exchange processes in the biopore-matrix scale (center) and soil macroscopic retention and shrinkage functions at drilosphere scale (left). The x, y, and z axes specify the location of the DEM-2PFV model.

that were implemented in the open-source software YADE (Šmilauer et al., 2015). Deformations and stresses in porous media that occurred during drainage events have been described, including the transition from the single- (water saturated) to the two-phase flow system, in the form of pendular bridges (Yuan and Chareyre, 2021). The latter authors suggested the term "two-phase pore-scale finite volumes coupled with the discrete element method" (DEM-2PFV) for such model scheme to solve quasi-static hydro-mechanical problems.

However, when applying the DEM-2PFV approach key challenges arise to identify the parameters in the constitutive laws that govern soil mechanical behaviour and to establish relationships between DEM-2PFV model micro parameters and measurable macro properties of soil. This process of parameterisation (Barbosa et al., 2020) can be time-consuming or even unpractical, depending on the complexity of the constitutive law and interactions among the parameters. For this, machine learning has shown to be efficient in finding correlations between microscopic parameters to be inserted in numerical modelling, and macroscopic parameters obtained empirically (Klejment, 2021) and may be a solution for parameterization of problems that integrate hydraulic-mechanical properties of soils. The use of machine leaning models also allows to calculate the importance of each micro parameters on the macro properties (Barbosa and Gerke, 2022). With this, one may quantify the role of specific mechanical properties (e.g. stiffness and cohesion) to withstand the structural stresses caused by hydraulic pressure.

The effective stress formulation (Bishop, 1960) includes the mechanical action of the pore water pressure on the soil solid phase. When plotting the stress against strain (e.g. uniaxial test), the slope of this plot can be interpreted as the stiffness and can be divided into two different stages (Wu et al., 2016). The primary stage is related to the elastic compression of the soil structure, and the secondary stage is related to aggregate rupture (i.e. bulk plastic deformation) (McDowell and Bolton, 1998; McDowell and Bono, 2013) and present higher stiffness (Wu et al., 2016). From the perspective of DEM-2PFV model parameterization, the slope of the primary and secondary stages may be parameterized by a combination of micro parameters of the constitute law governing the elasto-plastic behaviour arising from the interaction between particles. The soil bulk elasticity is reportedly calibrated by the particle stiffness in the DEM model (Coetzee and Els, 2009), while the aggregate rupture (i.e. plastic behaviour) (Cil and Alshibli, 2012) of the secondary stage may be calibrated by the bond strength among particles (Barbosa et al., 2020).

Therefore, to capture the highly dynamic plasma and structural porosity in nonrigid soils (Peng and Horn, 2005; Schäffer et al., 2013) due to inherent solid phase shrinkage-swelling or soil fracturing, it is essential for the numerical model to take into account a pore system that is structured in aggregates forming a partially-connected network of inter- and intra-aggregate pores. Thus, the effective stress may lead to aggregate breakage and displacement, altering the pore network and releasing particles that are magnitudes smaller than those of the soil matrix as in Barbosa (2020), and can be dragged through macropores in the drying process, for example. The spatial heterogeneity of the mechanical properties within the aggregates that form the matrix and coating material must be considered. Although the concept of soil aggregation has been criticized (Vogel et al., 2022), it is believed that this approach could be useful as a first attempt to analyse hydro mechanical coupled processes at the pore-scale level.

We hypothesise that besides reducing hydraulic conductivity, the higher stiffness and cohesion forces of the cementing agents present in finer particles forming the coating material, dampens the radial shrinkage of biopore samples, when compared to macropores of the aggregated matrix structure without the coating material. However, to investigate such a proposition we assumed that the macro parameters of the primary and secondary stress–strain stages, obtained from the experimental data, may be correlated with the micro parameters of the pore scale model. The objective was to develop and test a poly-dispersed DEM-2PFV model to mimic the pore structure of the coated biopore and surrounding aggregated soil matrix to simulate dynamic hydro-mechanical processes during flow exchange. To achieve the goal we i) carried out drainage experiments on samples with coated biopores, ii) mimicked the coating and soil matrix materials by differently-sized aggregates in form of a poly dispersed DEM-2PFV model, and iii) parameterized and quantified the importance of each mechanical property (i.e. particle stiffness and bond strength) on the shrinkage curve of each sample treatment.

2. Material and methods

2.1. DEM model of the structured soil around worm burrows

The solid phase of the soil matrix was created in three steps. The first was the discharge of spherical particles of 1 mm and 0.4 mm in diameter with a mass flow rate of 1.5 10^{-5} kg s^{-1} in a cuboid packing of 10 × 10 × 10 mm^3. Such mass flow rate produced a proportion of larger and smaller particles similarly to the amount of sand (549 g kg^{-1}) and clay (185 g kg^{-1}) in the Bt-horizon of a Haplic Regosol (haRG) soil profile (Rieckh et al., 2012). In total, the porous medium was formed by 683 and 3590 particles of 1 mm and 0.4 mm in diameter, respectively, randomly distributed in the cuboid. The second step was to create aggregates, thus, two spherical shells were created, one with 1 mm diameter and another with 0.4 mm diameter. In the first, 3600 particles with 0.052 mm in diameter were created inside, and in the second 1260 particles with 0.03 mm in diameter were created inside. Lastly, the third step was to replace each particle in the cuboid created in the first step by the respective aggregate from the second step.

The assembled cuboid packing of aggregates was compressed until the soil matrix porosity reached a similar value as observed in soil samples (see section 3.1). Then, due to computational limitations for the drainage simulations, the size of the initial packing was cropped, extracting a smaller cuboid of 5 × 5 × 5 mm^3 from the centre of the original one (Barbosa, 2020). The smaller packing contained approximately 25,000 primary particles with a diameter of 0.052 mm and 54,000 primary particles with a diameter of 0.03 (Fig. 2a).

For the coating, a DEM model of the solid phase was created within a random cuboid packing of dimensions 5 × 0.25 × 5 mm^3. Approximately 60,000 particles of 0.015 mm in diameter were used for the coating in order to present a relatively homogeneous material, different from the soil matrix. The coating pack was compressed until the porosity reached a value similar to the measured one and assembled at the bottom of the soil matrix packing (Fig. 2a).

The open-source software YADE (Šmilauer et al., 2015) was used for DEM modelling; the contact law definitions, scene construction, simulation control, and post-processing of data was carried out using Python programming language. A default contact law, already implemented in YADE (Scholtès and Donzé, 2015), accounted mainly for cohesive frictional material, more likely to reproduce the ductile rupture of wet aggregates. The heterogeneity of particle binding forces within the aggregate was done by setting an initial value of bond strength (see parameterization method in section 2.6) and the variation controlled by setting the shape parameter of the Weibull distribution to 1.5 (Barbosa et al., 2022b). The cohesive frictional contact law (Scholtès and Donzé, 2012) allowed to record the breakage of the bonded contact location, the instant when a particle contact was broken, and to quantify the orientation of the normal vector to the crack plane. The number of these cracks was calculated for each pressure increment. For all simulations, a global viscous damping of 0.1 was used to dissipate kinetic energy.

2.2. Two-phase pore scale finite volume (2PFV) coupled with DEM

The regular Delaunay facets and Voronoi vertices obtained from the Regular Triangulation method (Chareyre et al., 2012) defined pore bodies and throats within the poly-dispersed sphere-packing as shown in

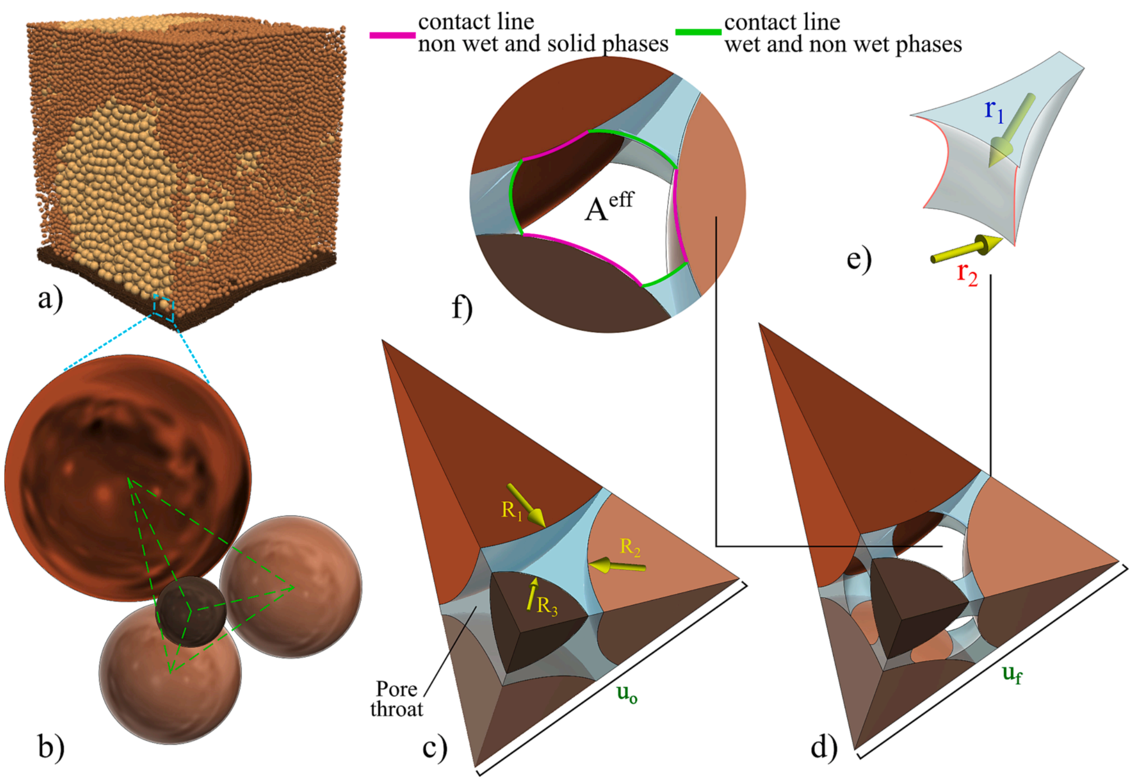

Fig. 2. Model of soil solid phase and pore network. a) Pack of soil matrix aggregates and particles of the coating material. b) Creation of regular triangulation. c) Tetrahedron defining pore geometry in a saturated condition. R_1, R_2 and R_3 are the radii of solid phase particles. d) Pendular bridges and the distance between the centres of solid particles, before (u_o) and after (u_f) drainage. e) Meniscus curvature during pore drainage, r_1 and r_2 are the principal radii of curvature.

the tetrahedron in Fig. 2b and c. The triangulation of the packing was performed by the open-source library CGAL (Pion and Teillaud, 2011). This procedure results in a mesh that accounts for local pore geometry (i. e. radii of solid phase and effective entry pore throat area, A_{eff}) which is linked to the dynamics of the solid structure (Fig. 2d, e and f). The elements of the mesh define the finite volume of the pore-network model and the local pore geometry is used for calculations of fluxes between the connected tetrahedral elements in function of pore pressure gradient (Chareyre et al., 2012).

The drainage process is controlled by gradually decreasing the capillary pressure (p_c), which is the pressure difference between the air (p^n) and water phases (p^w). The initial state of the packing was assumed to be water saturated. The pressure difference between air (non-wetting) and water (wetting) phases was achieved by setting an air pressure $p^n = 0kPa$ on the top of the packing, and the initial water pressure of $p^w = 0kPa$ at the bottom boundary. The drainage started by gradually decreasing p^w and keeping p^n constant (i.e., increasing p_c stepwise). The pressure step was 0.05 kPa until a maximum of 10 kPa was achieved; in this range there was a significant reduction in the water content for the soil used here (Rieckh et al., 2012). After each pressure step at the bottom boundary, the packing was allowed to stabilize and the forces to equilibrate. The mesh of the triangulation was updated according to the particle movement before the next pressure step was applied.

For this approach, the grains were considered perfectly wettable and the viscous effects in the fluids to be negligible. Pore water drainage was assumed to start when p_c is higher than the entry capillary pressure given by the pore throat geometry. With this, draining process may happens in more than one pore at once (Yuan and Chareyre, 2021). Moreover, the air or water could become disconnected from their reservoirs (in the top or bottom, respectively), which means that both phases are allowed to become trapped within the other. The 2PFV model is briefly reviewed below.

The air–water interfacial tension (γ) and geometry of the particles in contact (Fig. 2d and f) were used to calculate the maximum value of p_c, defined as entry capillary pressure (p_c^e), through Young-Laplace equation:

$$p_c = \gamma\left(\frac{1}{r_1} + \frac{1}{r_2}\right) \tag{1}$$

where r_1 and r_2 are the principal radii of the curvature of the meniscus (Fig. 2e).

Since it is difficult to obtain the values of r_1 and r_2, the entry capillary pressure (p_c^e) was determined based on the Mayer–Stowe–Princen (MS-P) method, which employed the balance of forces $\vec{F}$ exerted on a wet – non wet interface of each pore as:

$$\sum \vec{F}(p_c) = \vec{F^c}(p_c) + \vec{F^t}(p_c) \tag{2}$$

where, $\vec{F^c}$ is the capillary force acting on pore throat section domain (Fig. 2c); $\vec{F^t}$ is the total tension force along multi-phase contact lines (Fig. 2f), and p_c^e is the value of p_c such that $\sum \vec{F}(p_c) = 0$. The pore scale capillary force $\vec{F^c}$ is described as:

$$\vec{F}^{c}_{i,j} = \int_{\Phi_i \cap S_{i,j}} \left(p_i^n - p_j^w\right) \vec{n}\, ds = A_{i,j}^{eff}\left(p_i^n - p_j^w\right) \vec{n} \tag{3}$$

where Φ_i is the part of the tetrahedra occupied by nonwetting phase, $S_{i,j}$ is the common facet linking tetrahedron i and j and n is the normal vector to the surface element ds.

The pressure p_i^n is the nonwetting phase pressure of tetrahedron i and p_j^w is the wetting phase pressure of tetrahedron j, and $A_{i,j}^{eff}$ is the effective entry pore throat area. The tension force $\vec{F^t}$ is described as:

$$\overrightarrow{F}^{t}_{i,j} = \int_{\partial^{w}(\Phi_i \cap S_{i,j})} \gamma^{nw} \overrightarrow{t}\, dl + \int_{\partial^{s}(\Phi_i \cap S_{i,j})} \gamma^{ns} \overrightarrow{t}\, dl - \int_{\partial^{s}(\Phi_i \cap S_{i,j})} \gamma^{ws} \overrightarrow{t}\, dl \quad (4)$$

where, ∂ is the contour in contact with wet (w) and solid (s) phases (Fig. 2f), and where γ^{ns}, γ^{nw} and γ^{ws} are multiphase interfacial tensions related by:

$$\gamma^{ns} = \gamma^{nw} cos\beta + \gamma^{ws} \quad (5)$$

with β the contact angle of assumed to be zero here.

The total force on particle k is obtained by summing interfacial tension and pressure forces from all incident facets and contact lines:

$$\overrightarrow{F}^{k} = \Sigma \left[\overrightarrow{F}^{c.k}_{i} + \overrightarrow{F}^{t.k}_{i,j} \right] \quad (6)$$

More details on the development of solid phase force equations can be found in Yuan and Chareyre (2017).

2.3. Site and soil sampling

For testing the model, soil samples were collected from the Bt horizon (sand, silt, and clay contents of 55, 27 and 19 %, respectively, and a soil organic carbon content of 0.44 %) of an eroded Haplic Luvisol located in the hummocky arable soil landscape of the Uckermark region in northeastern Germany (53°23′ N, 13°47′ E). At this site, soil hydraulic and other properties have been intensively studied before (e.g., Rieckh et al., 2012). The area was characterized by an average annual precipitation of 489 mm and an annual mean air temperature of 8.6 °C, recorded at the Dedelow Experimental Field Station of the Leibniz Centre for Agricultural Landscape Research (ZALF), Müncheberg (https://www.zalf.de).

After excavating a soil pit down to the surface of the Bt horizon (Fig. 3a) the rectangular top surface area of 1 m × 2 m (Fig. 3b) was vacuum-cleaned and the earthworm burrows identified for counting the number and for diameter measurement. Around projected intact block with worm burrows, the soil at the sides around blocks was carefully

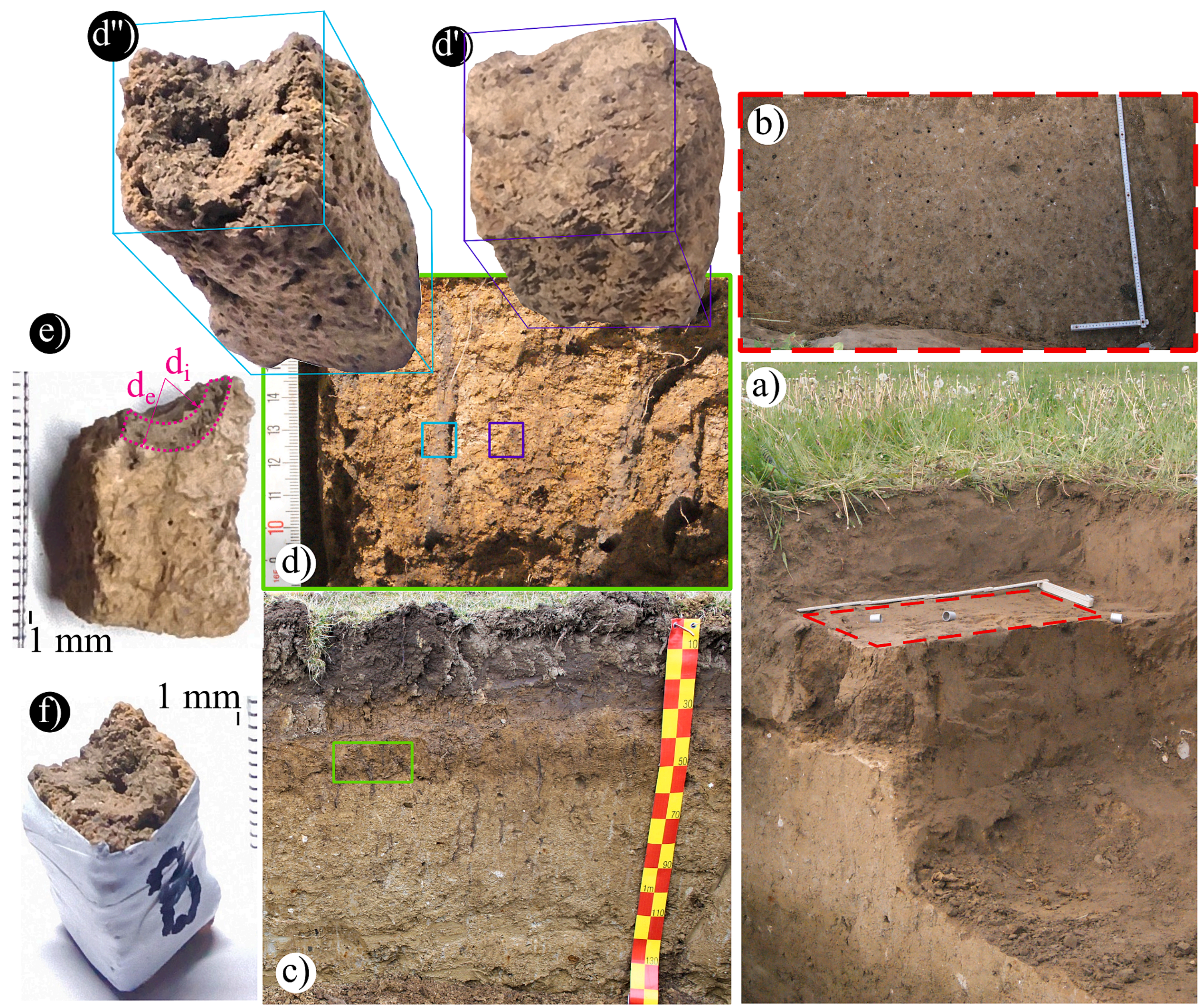

Fig. 3. Sample location and preparation. a) Pit excavated in the Bt soil horizon. b) Top view of Bt horizon showing the earthworm burrows. c) Lateral view of the soil profile wit vertical earthworm burrows. d) Detail of the surface of earthworm burrow observed in the soil profile. d') Isometric view of a matrix sample. d'') Isometric view of a coated sample, cubes of approx. 10 mm edge. In front, the coated surface of earthworm burrow. e) Lateral view of the coated sample, the earthworm burrow inner diameter (di) was between 4 and 6 mm and the outer diameter (de) was between 5 and 8 mm. The coating thickness was calculated from de and di. f) Sample stabilized with PTFE tape for the sand box experiments.

removed (i.e., cut laterally) in order to better access the intact earthworm burrow surfaces (Fig. 3c and d) show details of this procedure. Once the burrows were identified, the burrow structure collected and cubic samples of approximately 10 mm were extracted from it, where one face of the cube presented the coated earthworm burrow (Fig. 3d''). These samples were identified as "coated samples", hereafter. The same procedure was performed to extract cubic soil matrix samples adjacent to the burrow, but without the coating surface (Fig. 3d'). These samples were identified as "matrix samples", hereafter. Both, coated and matrix samples were stabilized with three turns of polytetrafluoroethylene (PTFE) tape along the side of the cube leaving the top and bottom open (Fig. 3e and f). The tape should prevent the sample from disruption during handling and from lateral evaporation.

2.4. Sample preparation

For sample preparation and separation of coating material of burrow walls from the soil matrix (Fig. 4a), a fossil preparation chisel (ZOIC PalaeoTech, Longburton, UK) and the engraver Dremel-290 were used with vibrations of 7.7 ms^{-2} and frequency of 100 Hz (Fig. 4b and c). The chisel was manually placed at the interface between coating and matrix characterized by the colour difference. Thus, the imposed vibrations generated elastic waves creating concentration of tension which creates a moving crack front. The crack propagation spread (Morrissey and Rice, 1998), splitting materials with contrasting mechanical stability such as between matrix and organo-mineral components in the coating (Peng et al., 2011).

From the separated coating material (i.e., several pieces of clods with intact coating, c.f. Fig. 4c) the density of 20 pieces and 20 matrix cubic samples were determined using the pycnometer GeoPyc 1360 (Micrometrics, Norcross, Georgia, USA). The GeoPyc machine uses a chamber filled with rigid microspheres with dry lubricant, increasing the fluidity of the powder-like spheres and ensuring complete wrapping of the soil sample. The chamber diameter was 25.4 mm and the volume of powder was kept constant for all measurements. Before running the measurements on soil samples, stones (quartz) with similar size and shape and known volume were used for calibration and determination of the conversion factor to be used for measurements of the soil clods. Each measurement started with the determination of the powder volume without the soil sample. Then, clod samples were inserted in the chamber together with the powder and the combined volume was determined. The volume of the samples resulted as the difference between the two measurements. In order to maintain the repeatability, a uniform consolidation force of 51 N was used in all measurements. A soil particle density of 2640 kg m^{-3} was assumed (Rieckh et al., 2012) and used together with bulk sample density to calculate the porosity of coating and matrix.

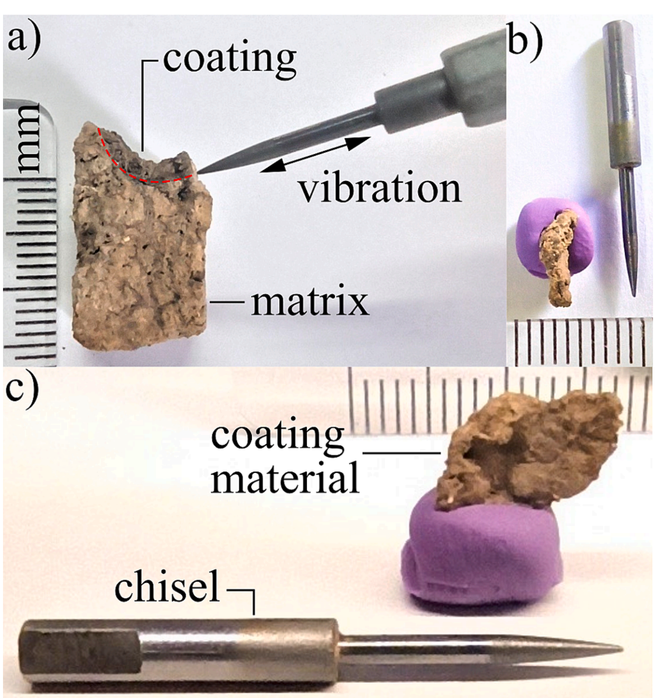

Fig. 4. Splitting coating material from soil matrix. a) Identification of the coating and positioning of the oscillatory chisel. Red dotted line is the interface between matrix and coating material. b) Top view from the splitted coating material and the chisel. c) Lateral view of coating material and the chisel. (For interpretation of the references to colour in this figure legend, the reader is referred to the web version of this article.)

2.5. Drainage experiments in sand box

The drainage experiments were designed to promote water movement from soil matrix through the coated burrow surface (Fig. 3e and f). Thus, the samples were placed in the sand box with the coated burrow in contact with the sand layer. Since the coated samples presented a curved surface due to the earthworm burrow, the sand box surface had to be prepared with a curved shape in order to guarantee full contact between coated surface and the sand (Fig. 5a). The maximum height, h, of this curved shape (Fig. 5b) was approximately 2 mm. The matrix samples were placed in the sand layer over a flat surface also 2 mm high to ensure both samples were in the same initial level. In order to minimize effects of structural anisotropy on the results, the same sample orientation as collected from field, was maintained parallel for matrix and coated samples (Fig. 3d).

The matrix and coated cubic samples were assembled under control of an optical-laser sensor (scanControl 2700-100, Micro-Epsilon) (Fig. 5a). A tensiometer T5 was also placed in the sand box to track pressure head over time. The frequency of acquisition for the optical-laser sensor was 10 Hz and the tensiometer acquisition was 0.2 Hz. The sand box was set to a pore pressure of −9.5 kPa, and the samples positioned under the optical-laser sensor field. Then, the water level in the sand box was raised until it reached 0 Pa, this process lasted 120 s. Due to the water uptake, the samples started to swell, which was measured by the optical-laser sensor. Once the sample stabilized after swelling-induced movement ceased, the water level was successively lowered in the sand box. The pore pressure was reduced at a rate of approximately 50 Pa s^{-1}. During this process the 2D-optical-laser sensor monitored the height of the sample's surface profile, and the data were evaluated using the software scanCONTROL Laserscanner 2D, Micro-Epsilon, to calculate the true strain ε, of the sample over time as:

$$\varepsilon = \ln(1 + e) \quad (7)$$

where e is the engineering strain (ratio between the height variation and the initial height of the sample), directly obtained from the sample deformation.

In total, 80 samples were used in these measurements, 40 samples of each treatment. The laser sensor was set to horizontal resolution of 640 points $profile^{-1}$ and vertical resolution of 0.003 mm.

The moving average of the data from the true strain (ε) was plotted against the pressure head obtained from the tensiometer. This plot was divided in two linear segments, the first with equation $f(x_{emp}) = a_{emp}x_{emp}$ and the second segment with equation $f(x_{emp}) = b_{emp}x_{emp} + c_{emp}$, where x_{emp} is pressure head from the tensiometer and $f(x_{emp})$ is the true strain calculated from the laser sensor.

2.6. Model parameterization and calibration

A number of 250 drainage simulations were carried out using a constant soil matrix structure and randomly varying the particle stiffness

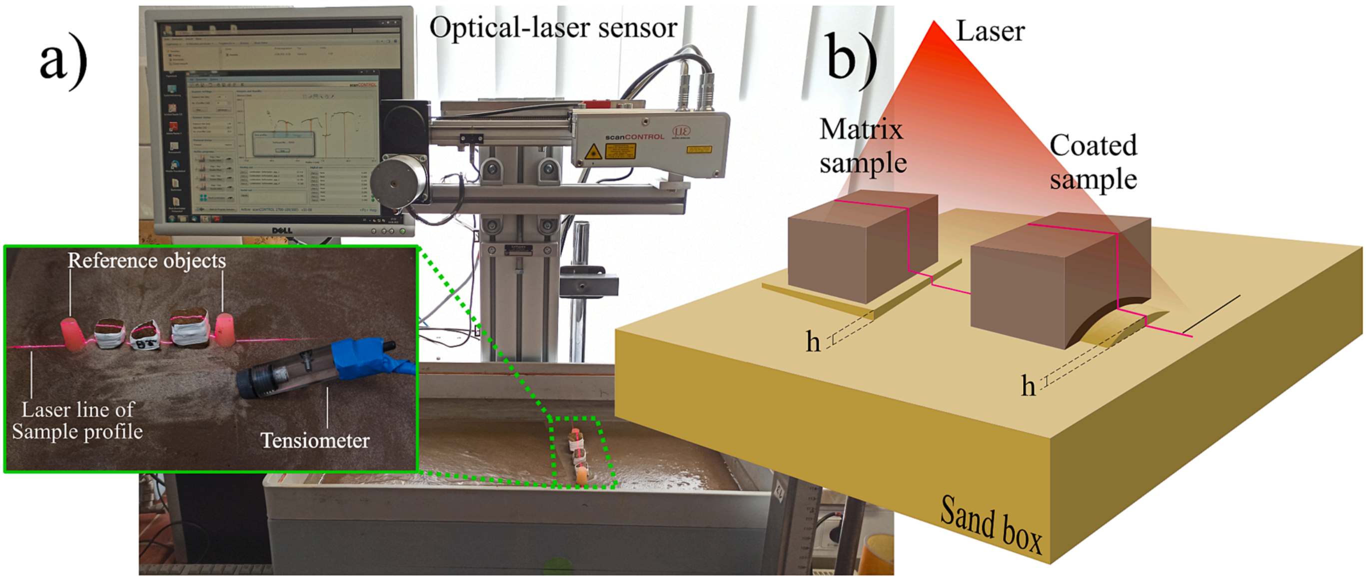

Fig. 5. Experimental configuration of sand box and optical-laser sensor. a) Arrangement of samples to quantify the shrinkage curve and the pressure head. b) Measuring sample shrinkage using optical-laser senor. The detail of sand box surface shows the sand arrangement for matrix and coated samples (h ~ 2 mm).

and bond strength between values of 6e6−9e6 Pa and 400–1000 Pa, respectively. These values were chosen to cover a wide range of possible solutions. In these simulations, saturation, fluid velocity, porosity, strain and crack surface area were quantified along with the pressure head. As was done experimentally, the plot strain versus pressure head was divided in two linear segments, the first with equation $f(x) = ax$ and the second segment with equation $f(x) = bx + c$, where x is pressure head and $f(x)$ is the true strain.

The micro parameters (i.e., particle stiffness and bond strength) from the constitutive law of particle interaction, were defined as independent parameters. The three macro parameters (i.e., a $[Pa^{-1}]$, b $[Pa^{-1}]$, and c $[-]$) were quantified for each combination of micro parameters, and defined as dependent parameters. Machine learning was employed to find the dependency network between microscopic (independent variable) and macroscopic (dependent variable) parameters. The DEM-2PFV simulation dataset was used to train multi-output regression with random forest *meta*-estimator (Pedregosa et al., 2011). Here, the DEM-2PFV dataset was randomly divided into the training and test part in a proportion of 80% and 20%, respectively. The performance of the *meta*-estimator algorithm was evaluated by the relationship (R2) between predicted and observed numerical data. In Random Forest, the depth of a variable used as a decision node in a tree can be used to assess the relative importance of that variable in predicting the output. Therefore, the importance of particle stiffness and bond strength to predict the macro parameters a, b, and c was evaluated.

With the trained *meta*-estimator algorithm, a non-linear optimization was performed in order to obtain the micro parameters (i.e., particle stiffness and bond strength) from the constitutive law of particle interaction that reproduce the average values of the macro parameters obtained empirically (i.e. a_{emp}, b_{emp}, c_{emp}) and its respective standard errors were used to calculate upper and lower limits. Thus, with a given initial estimation of micro parameters (i.e., particle stiffness and bond strength), the optimization started with the estimation of the macro parameters obtained from the trained algorithm (a_{pred}, b_{pred}, c_{pred}) and compared with macro parameters obtained empirically (i.e. a_{emp}, b_{emp}, c_{emp}). In order to obtain the final estimation from a global minimum with little error, the initial estimation should be in the close vicinity of the correct value of the parameters (Asaf et al., 2007). The optimization process stopped when the best combination (minimum error of objective function) of the particle stiffness and bond strength was achieved. Thus, the objective function (*OF*) was:

$$OF = \frac{1}{3}\left|\left[\frac{(a_{pred} - a_{emp})}{a_{emp}}\right]\right| + \left|\left[\frac{(b_{pred} - b_{emp})}{b_{emp}}\right]\right| + \left|\left[\frac{(c_{pred} - c_{emp})}{c_{emp}}\right]\right| \quad (8)$$

where $a_{pred}[Pa^{-1}], b_{pred}[Pa^{-1}], c_{pred}[-]$ are the macro parameters of the strain-pressure head curve obtained by the combination of particle stiffness and bond strength in the trained algorithm and $a_{emp}, b_{emp}, c_{emp}$ are those of the strain-pressure head curve obtained empirically.

This optimization process was performed for the average values of the macro parameters as well as for the upper and lower limits given by the standard errors (se). The parameterized micro parameters spatialized for each particle contact (i.e., particle stiffness and bond strength) obtained for the soil matrix were used for the coated sample. Once again, 250 drainage simulations were carried out using the soil matrix structure, but now combined with the coating material. The particle stiffness and bond strength of the coating material were randomly varied between 6e6-22e6 Pa; and between 2e5-10e13 Pa, respectively. The dependent and independent variables were then used to train the multi-output regression with random forest *meta*-estimator (as presented above) and all the parameterization processes were repeated.

2.7. Pore network calculation

Particle contact was analysed throughout the simulation. When there was a break in the binding force, then the model started to quantify the relative movements between particles. If the relative movement indicated a separation between the particles, then this point was considered as a crack formation. The binding force can be restored if the particles come into contact again. Pore throats were calculated using the Delaunay facets and Voronoi vertices obtained from the Regular Triangulation method (Chareyre et al., 2012) within the poly-dispersed sphere-packing (Fig. 2b and c).

The pore geometric tortuosity (τ) of each sample from numerical simulation were calculated based on pore distance map obtained from Fiji (Schindelin et al., 2012) (voxel size 3 μm × 3 μm × 3 μm), which quantified the length of the skeleton (actual path length - ξ) for each pore and the Euclidian distance, and tortuosity was calculated as the ratio between ξ and the Euclidian distance. Also from the distance maps (Legland et al., 2016), the inner pore structure of aggregates and the pore between aggregates (inter aggregate pores) were obtained. From a section of the packing, the section area of inter aggregate pores (S_{inter}) was calculated to track the expansion or retraction of pre-existing macropores. The same section location was considered for the matrix and coated sample, allowing comparison of the effect of the coating material on the structural behaviour of the pores. Both measures (τ and S_{inter}) were taken from different pressure heads in order to provide information about the evolution of the simulated pore network.

3. Results

3.1. Density of soil samples and pore throat size distribution of DEM packings

The average bulk density of the soil matrix samples and the bulk density of the coating material are summarized in Table 1. The particle density was considered 2.64 g cm^{-3} (Rieckh et al., 2012) for both materials. The porosities of the matrix packing composed by aggregates and the coating packing obtained in DEM are also in Table 1.

Also from the DEM model, the pore throat size distributions of the entire pack of matrix and coated sample for the initial condition of the structure are presented on Fig. 6. From both samples three main pore sizes were found, i - the inter aggregate pore throat ($P_1 > 1e\text{-}4$ m), ii – pore throat within the 1 mm aggregate ($1e\text{-}4 < P_2 < 1e\text{-}5$ m) and iii – pore throat within the 0.4 mm aggregate ($1e\text{-}5 < P_3 < 1.3e\text{-}6$ m). Additionally, the coated sample presented a pore throat within the coating material ($P_4 < 1.3e\text{-}6$ m).

3.2. Training the random forest (RF) meta-estimator and model parameterization

The RF best fit was found for the number of estimators set to 200, maximum depth set to 50 and random state to 2. The evaluation of R2-score for each macro parameter a^m_{pred},b^m_{pred} and c^m_{pred} for matrix sample and a^{cs}_{pred}, b^{cs}_{pred} and c^{cs}_{pred} for coated sample are presented in Fig. 7.

Table 2 summarizes the average and the upper and lower limits of the experimental macroparameters values (se) used by the objective function (Eq. (8)) obtained from the experimental curve strain – pressure head (Fig. 8) for matrix (a^m_{emp}, b^m_{emp} and c^m_{emp}) and for the coated sample (a^{cs}_{emp}, b^{cs}_{emp} and c^{cs}_{emp}) (Fig. 9) and the ones obtained by the simulations using the parameterized micro parameters from the trained *meta*-estimator algorithm with non-linear optimization (Figs. 8 and 9).

The trained RF *meta*-estimator combined with the experimental macro parameters resulted in an error obtained from the objective function of 0.4 and 0.3% for matrix and coated sample, respectively. From this process, the parameterization of numerical model micro-parameters to reproduce the average of the values of the experimental macro parameters and its upper and lower limits (given by the coefficient of variation - cv) resulted in particle bond strength of 870 Pa (cv 8.65%) and 500 MPa (cv 8.29%) for the aggregates in the matrix and coating material, respectively. The parameterized particle stiffness was 6.7 MPa (cv 8.02%) and 13.6 MPa (cv 16.07%) for the aggregates in the matrix and coating material, respectively.

The importance of each microparameter (particle stiffness and bond strength) in predicting each macroparameter is displayed on Fig. 7. The macro parameters from the matrix strain-pressure curve were mostly affected by particle bond strength, which values of feature importance were calculated as 0.98, 0.96 and 0.98 for a^m_{pred},b^m_{pred} and c^m_{pred}, respectively. However, the particle stiffness is the main micro parameter in predicting the macro parameters of coated sample. The values of importance were 0.97, 0.84 and 0.94 for a^{cs}_{pred},b^{cs}_{pred} and c^{cs}_{pred}, respectively. Particle bond strength presented a slight importance increment when predicting b^{cs}_{pred} (feature importance value of 0.16), when compared to a^{cs}_{pred} and c^{cs}_{pred}.

Table 1
The average bulk density of the soil matrix and coating material and porosity obtained in the model.

		Matrix (*se*)	Coating (*se**)
Empirical data	Bulk density [g cm^{-3}]	1.65 (0.15)	1.84 (0.15)
	Porosity [%]	37 (2)	30 (2)
Simulation data	Porosity [%]	42 (0.5)	33 (0.5)

**se* is the standard error.

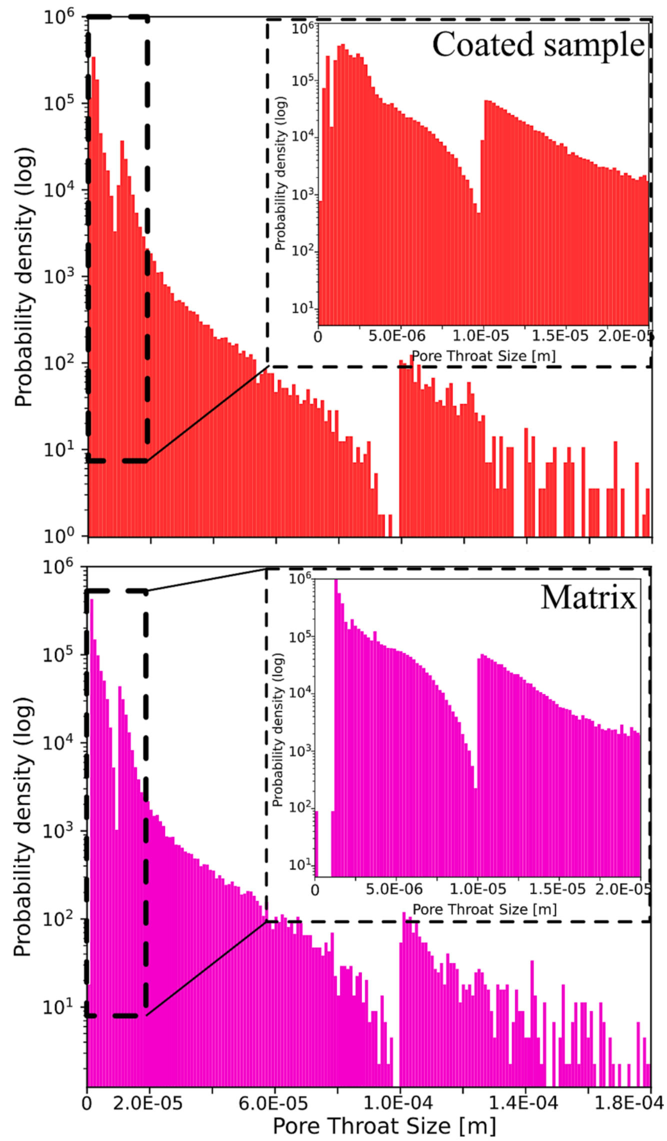

Fig. 6. Pore throat radius distribution of DEM packings of coated sample (up) and matrix (bottom). The three main pore sizes common to both samples are: i - the inter aggregate pore throat ($P_1 > 1e\text{-}4$ m), ii – pore throat within the 1 mm aggregate ($1e\text{-}4 < P_2 < 1e\text{-}5$ m) and iii – pore throat within the 0.4 mm aggregate ($1e\text{-}5 < P_3 < 1.3e\text{-}6$ m). Additionally, the coated sample presented a pore throat within the coating material ($P_4 < 1.3e\text{-}6$ m).

3.3. Pore network

The variation of pore network due to particle displacement and shrinkage is presented in Fig. 10a. The variation of section area of inter aggregate pores and geometric tortuosity alongside pressure head is presented in Fig. 10b and 10c. Both samples presented a maximum retraction in section area of inter aggregate pores around 3000 Pa, which was more significant for the matrix sample (c.a. 1.7e-2 mm^2). At

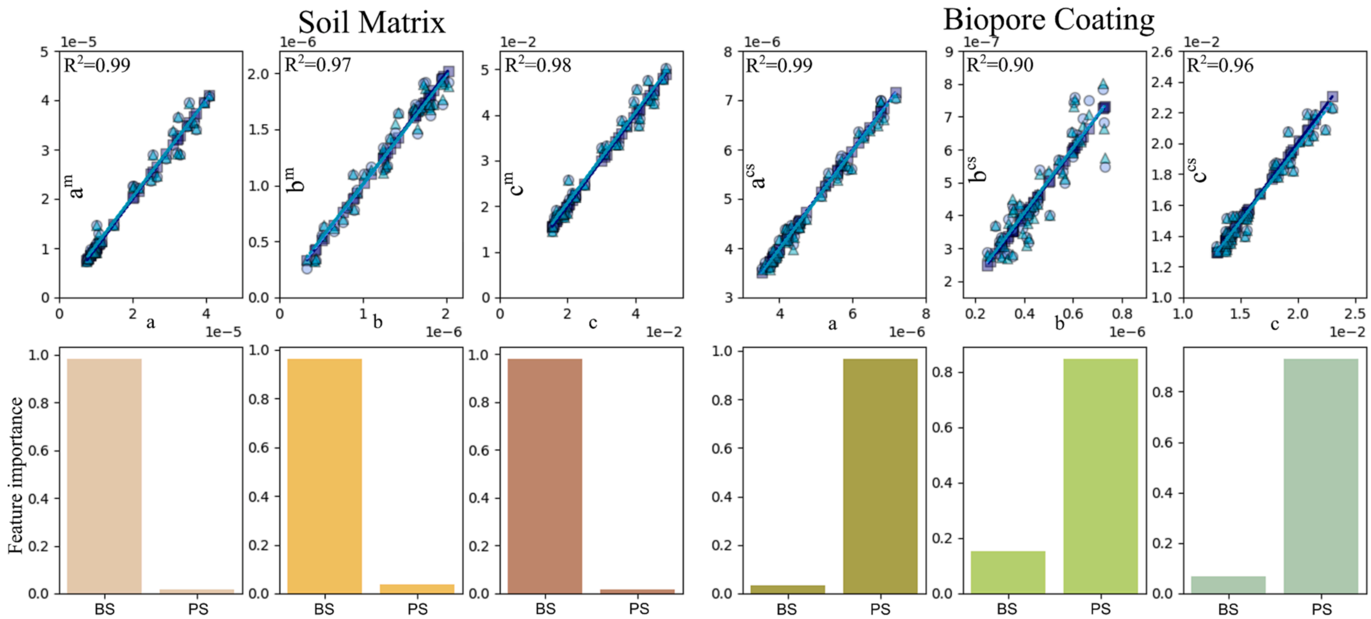

Fig. 7. Evaluation of random forest (RF) *meta*-estimator metrics and importance of each micro parameter (particle stiffness-PS and bond strength-BS) in the prediction of strain-pressure curve macro parameters (a $[PA^{-1}]$, b $[PA^{-1}]$ and c $[-]$) for each sample.

Table 2
The macro parameters obtained from the curve strain – pressure head experimental and numerically for the -matrix and for the coated sample. Standard error (se) indicates the upper and lower limits.

	Sample	Macro parameters					
		a $[Pa^{-1}]$	se (±)	b $[Pa^{-1}]$	se (±)	c $[-]$	se (±)
Empirical data	Matrix	2.36e-5	3.31e-6	1.38e-6	2.17e-8	3.50e-2	3.37e-3
	Coated	4.46e-6	3.91e-7	3.57e-7	7.78e-9	1.86e-2	2.57e-3
Simulation data	Matrix	2.34e-5		1.32e-6		3.36e-2	
	Coated	4.17e-6		3.56e-7		1.42e-2	

3000 Pa, the matrix sample had the lowest tortuosity value during drainage. Above 4500 Pa, both samples presented increment of section area of inter aggregate pores and tortuosity; however, the variation on matrix sample was once again more significant.

4. Discussion

4.1. Macro parameters of the strain–stress curve and DEM-2PFV parameterization

The drainage induced soil shrinkage resulted from a combination of aggregate compression and breakage (Figs. 8 and 9). Simulations show the majority of aggregate compression during the primary compressive stage, as evidenced by the higher particle displacement velocity in Figs. 8 and 9. This behaviour lasts up to the point of the crushing stress (Wu et al., 2016) - c.a. 1700 Pa for the matrix sample and 3000 Pa for the coated sample (Figs. 8 and 9). From this point onwards, the stress increment causes the greatest breakdown of the aggregates (Figs. 8 and 9). This triggers an immediate plastic yielding and hardening (Cil and Alshibli, 2012), and readily reduces the slope of the strain–stress curve, indicating the beginning of the secondary compressive stage.

The ability of soil to withstand internal stresses caused by decreasing water potentials during drying process is defined as hydro structural stability (Schäffer et al., 2013). The larger the hydro structural stability, the smaller will be the slopes of the strain–stress (i.e. pressure head) curve and the less it will shrink during drying (Boivin et al., 2006). Therefore, the higher hydro structural stability of the coated sample is quantified by the smaller slopes of the two compressive stages from strain-pressure head curve (Table 2). It is known that biological exudates can increase the binding forces among soil particles and therefore the overall mechanical stabilization (Peng et al., 2011). Consequently, the effective stress caused by the drying process (Bishop, 1960) led to a higher bulk deformation of the matrix sample (Fig. 8) when compared to the coated sample (Fig. 9).

In drying coated sample, the effective stress is in its majority distributed over the coating material and transmitted to aggregates in the matrix with less intensity (c.f. Video 1 in the additional material). This prevents aggregate breakage (c.f. smaller number of cracks, Fig. 9) and the deformation of the particles in the coating material prevails. Thus, the elastic effect of particle deformation is predominant thus, particle stiffness plays the major role in the bulk deformation (Asaf et al., 2007; Coetzee and Els, 2009). Therefore, particle stiffness of the coating material is the most important micro parameter that controls the macro parameters (Table 2) of the strain-pressure head curve obtained for the coated sample during drying process (Fig. 9), as shown by the Random Forest (RF) meta estimator (Fig. 7).

In drying matrix sample the effective stress is distributed only over the matrix aggregates (c.f. Video 2 in the additional material). In this case, the sum of capillary ($\vec{F^c}$) and tension forces ($\vec{F^t}$) (Eq. (2)) overcomes the particle bond strength, leading to further breakdown of the aggregates (c.f. higher number of cracks, Fig. 8). Thus, the plastic effect of aggregate breakage is predominant (Cil and Alshibli, 2012) and therefore particle bond strength, that governs aggregate rupture (Barbosa et al., 2020; Barbosa and Gerke, 2022; Mueller et al., 2017), plays the major role in the macro parameters (Table 2) of the strain-pressure head curve obtained for the matrix sample during drying process (Fig. 8), as

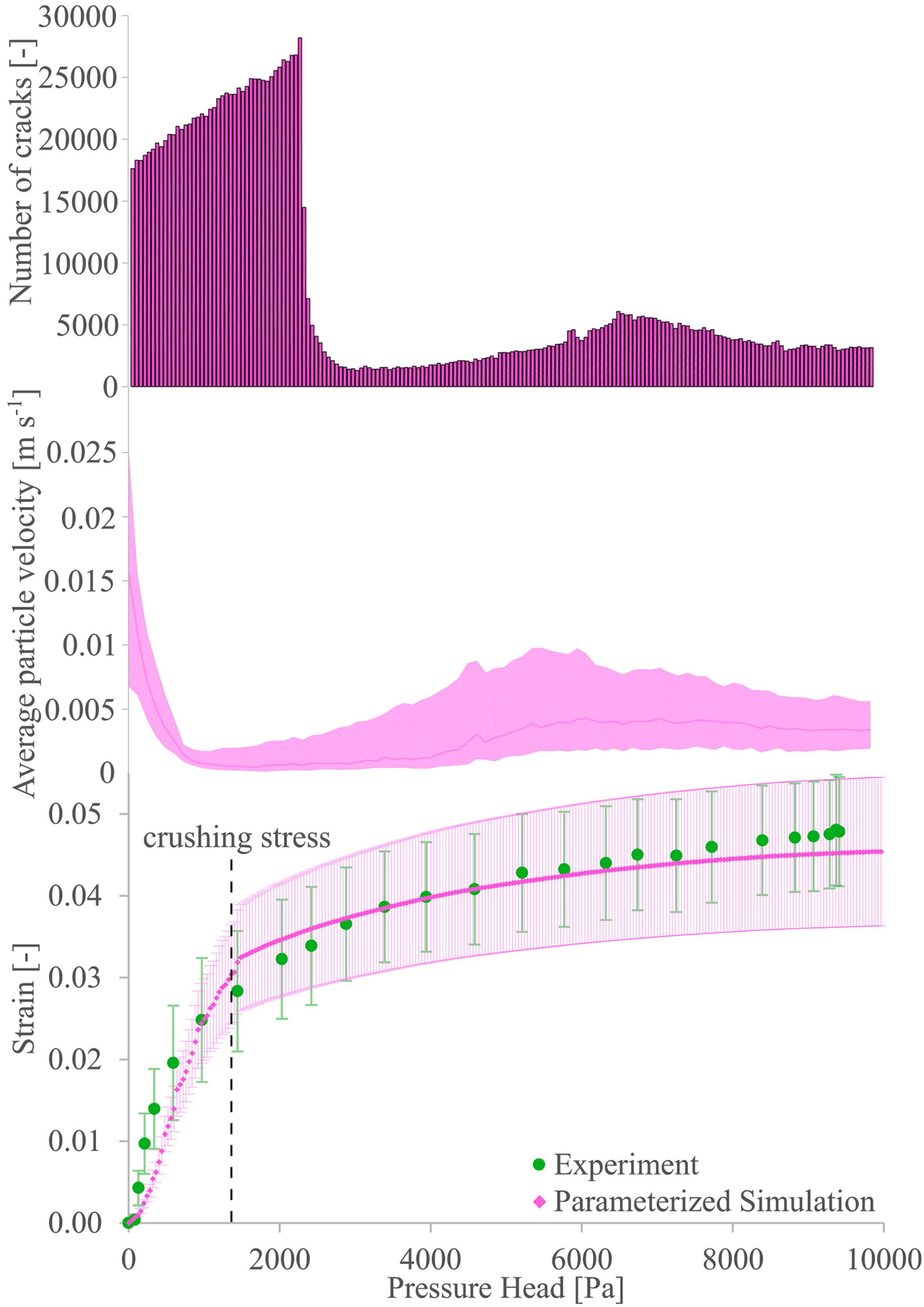

Fig. 8. Structural dynamics of the matrix sample. Bottom) Empirical strain-pressure head curve and the respective curve of the numerical model parameterized using the average values of the macro parameters (a, b and c), as well as the values of upper and lower limits (shaded envelope) obtained for the matrix sample. Middle) The average of particle displacement velocity with respective error (shaded envelope) and the number of cracks in each pressure head step (top) are plotted alongside the drainage process.

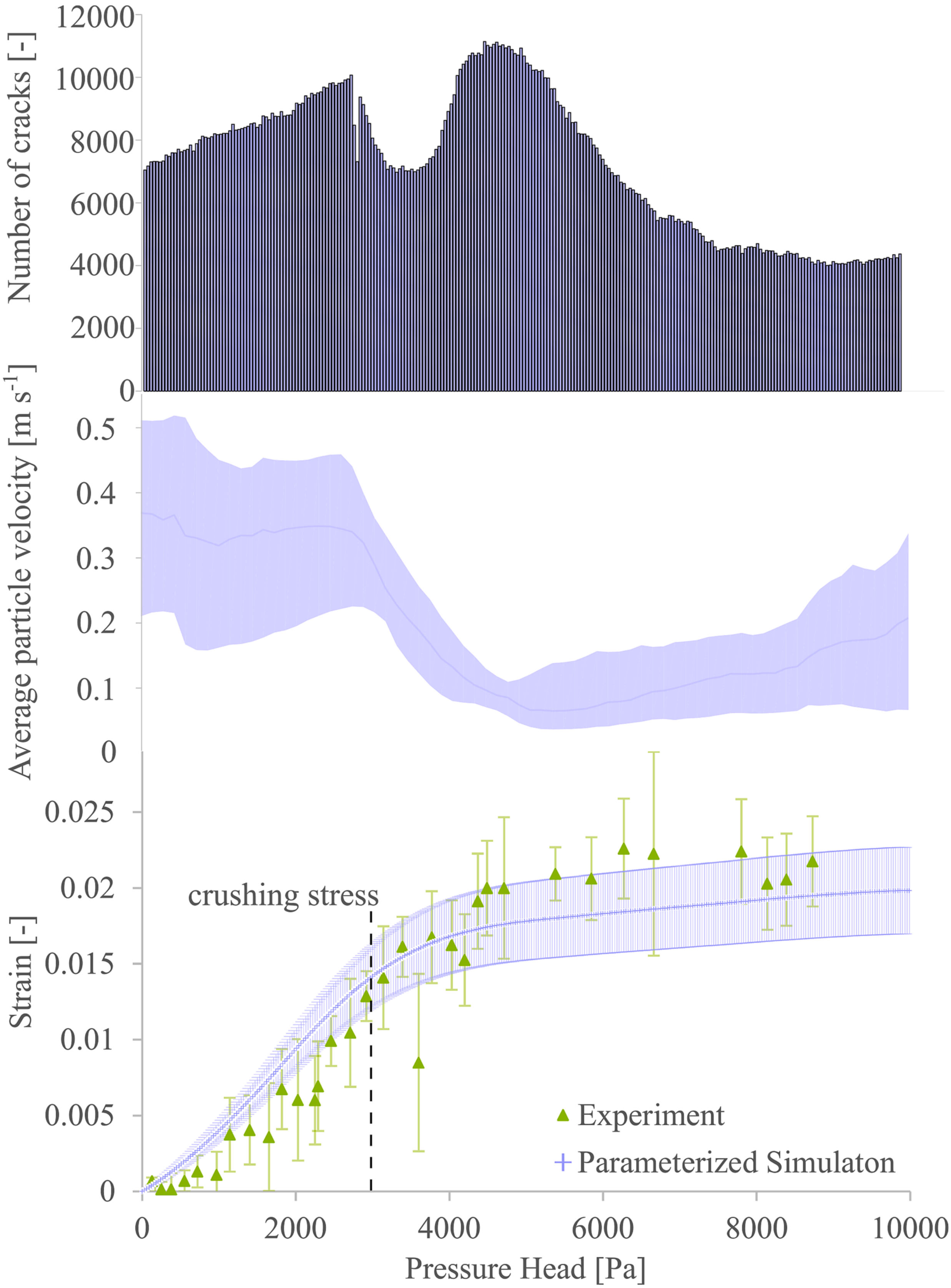

Fig. 9. Structural dynamics of the coated sample. Bottom) Empirical strain-pressure head curve and the respective curve of the numerical model parameterized using the average values of the macro parameters (a, b and c), as well as the values of upper and lower limits (shaded envelope) obtained for the coated sample. Middle) The average of particle displacement velocity with respective error (shaded envelope) and the number of cracks in each pressure head step (top) are plotted alongside the drainage process.

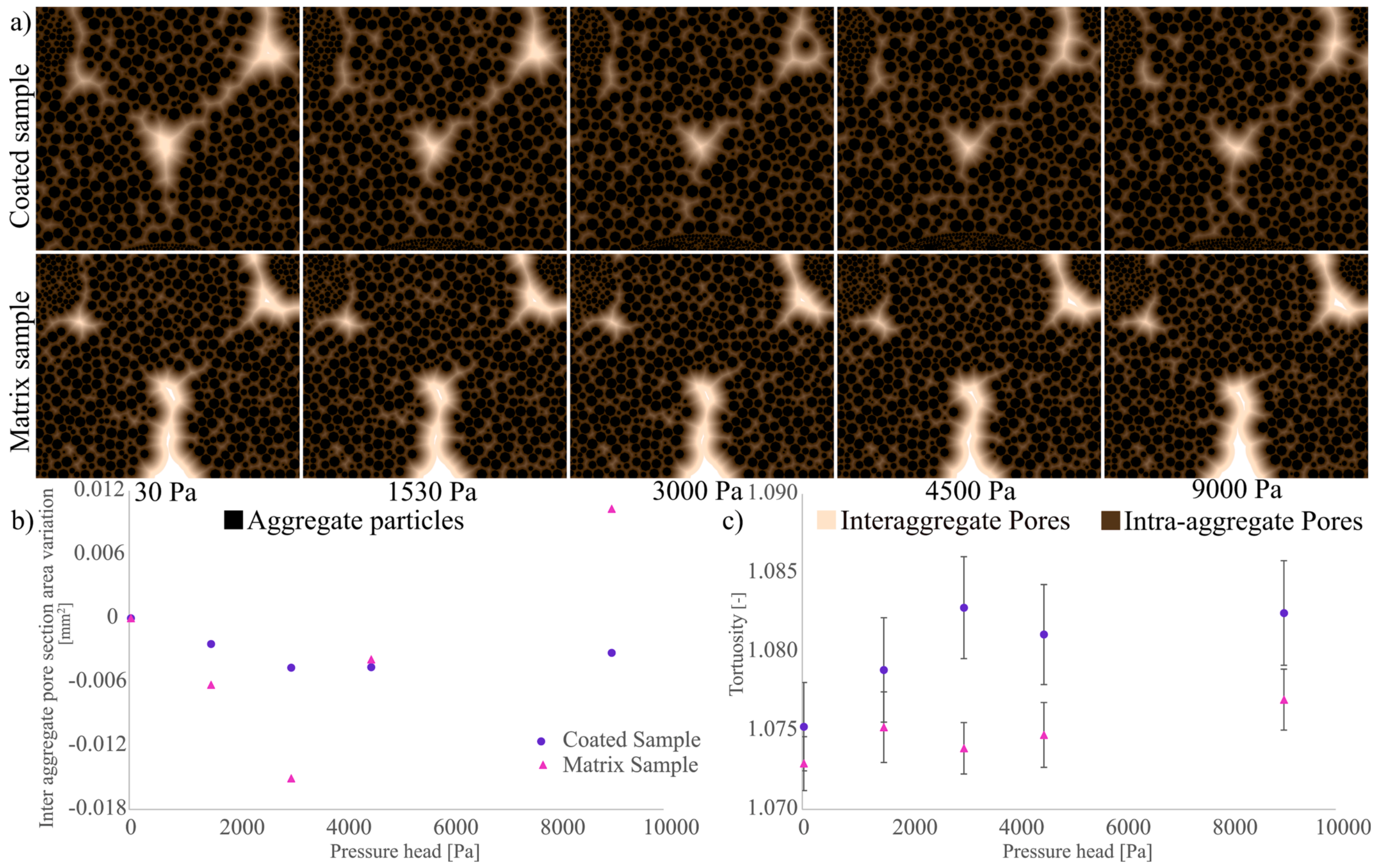

Fig. 10. Pore network dynamics for the simulations of drying samples. a) Image segmentation calculating the section area of inter aggregate pores. b) The negative and positive variation of the section area of the inter-aggregate pores in relation to its initial value indicate retraction and expansion of the porous structure, respectively, while increasing the pressure head. c) Tortuosity along with pressure head for both samples.

shown by the Random Forest (RF) meta estimator (Fig. 7).

Although the modelled pore network does not reproduce the experimental pore architecture, the approach introduces the concept of 3D pore structure formed by intra and inter aggregate gaps combined to organo-mineral interactions (i.e. characterized by the physical properties of the coating material) (Vogel et al., 2022). Each DEM-2PFV simulation was performed using 40 cores in parallel of a HPC cluster with a total of 5000 cores and 12 terabytes of RAM. In this configuration, DEM-2PFV simulation of matrix sample lasted 40 min, while that of the coated sample lasted 2 h. Moreover, it enlightens our initial assumption that the macro parameters of the primary and secondary stress–strain stages correlate with the micro parameters (particle stiffness and bond strength) of the pore scale of the model. Hence, the supervised machine learning could satisfactorily establish a prediction model with accuracy of the testing dataset (R2 metric) above 90% for all parameters (Fig. 7) to parameterize particle stiffness and bond strength of the matrix and coated sample of the DEM-2PFV model.

However, it is important to note that soil stiffness can be influenced by various factors, including soil texture and management practices (Keller et al., 2013), which means that when modelling different soil structures, the training *meta*-estimator algorithm needs to be repeated to ensure accurate predictions. A possibility to overcome this drawback would be to expand the variables used in the machine-learning procedure, including, in addition to particle stiffness s and bond strength, the proportion of particle size fractions (i.e., clay, sand, silt), cementing agents (i.e., organic matter), as well as porosity (Barbosa and Gerke, 2022).

4.2. Pore scale structure dynamics during drainage

Initially, samples in the numerical model were characterized by three main pore sizes i - the inter aggregate pore throat ($P_1 > 1e\text{-}4$ m), ii – pore throat within the 1 mm aggregate ($1e\text{-}4 < P_2 < 1e\text{-}5$ m) and iii – pore throat within the 0.4 mm aggregate ($1e\text{-}5 < P_3 < 1.3e\text{-}6$ m). Additionally, the coated sample presented a smaller pore throat within the coating material ($P_4 < 1.3e\text{-}6$ m) (Fig. 6).The internal forces, in the primary compressive stage of the matrix sample, derives predominantly from the loss of water between aggregates (Video 2 in the additional material), also defined as structural porosity (Schäffer et al., 2013). This stress overcome the forces acting on the inter-aggregate region that are smaller than the forces stabilizing the aggregate (Huang et al., 2011). This caused the displacement of aggregates (see higher particle velocity in Fig. 8), reducing the gaps among aggregates and consequently, the section area of inter aggregate pore shrunk (Fig. 10b). Similar result was observed for the coated sample (Fig. 10b), however at lower intensity (see particle velocity in Fig. 9) due to the presence of the coating material which increased the stiffness of the structure (Fig. 9) in agreement with Barbosa et al. (2022) and Schäffer et al. (2008b).

This hydro structural behaviour of higher deformation with drainage of structural porosity displayed by the matrix sample has been reported as interpedal shrinkage (Braudeau et al., 1999), while the drainage of structural porosity with lower deformation displayed by the coated sample has been named as structural shrinkage (Schäffer et al., 2013). In both cases, the bulk volume shrinkage is a result of pore network collapse (Bottinelli et al., 2016).

The drainage process can be seen in the Video 1 (coated sample) and 2 (matrix sample) in the additional material, where internal stresses together with saturation are presented dynamically in 3D for the matrix.

From the videos, lower values of internal stresses distributed within the solid phase can be observed for pressure head from 0 to c.a. 1700 Pa for matrix sample and 3000 Pa for coated sample, given the greater mobility of structure (i.e. aggregate deformation). After the crushing stress (Figs. 8 and 9) the structural mobility is reduced (see particle velocity in Fig. 9) and the internal stresses distributed within the solid phase started to increase (Videos 1 and 2). The increase in internal stresses led to a maximum breakdown of the aggregate (Figs. 8 and 9), from this point onward, the inter aggregate pore section area stabilized in the coated sample and started to increase in the matrix sample. Bottinelli et al., (2016) analysing the pore structure in soil shrinkage experiments, showed that in addition to pore network collapse, new pores can be formed during shrinkage due to the creation or expansion of pre-existing cracks during the drying process. This happens when the plasma porosity (Schäffer et al., 2013) (i.e. intra aggregate and coating pores, in our case) shrinkage is greater than the bulk soil deformation. The transition between the primary and secondary compressive stage till the end of the secondary stage encompasses the normal and residual shrinkage. This interpretation however, should be broken down into specific details in further investigations of upscale analysis of soil shrinkage curve (Fig. 1).

From the combined analysis of tortuosity increment and cross-section of inter aggregate pore network shrinkage (Fig. 10b and c), a reduction in the horizontal permeability (radially to the macropore) is expected during the primary compression stage for both soil treatments (Niya and Selvadurai, 2018). The quantification of the dynamics of secondary pore system network (van der Linden et al., 2019) linking the macropore surface and soil matrix (Le Mer et al., 2021), may be an important feature of the presented model to dynamically access the macropore-matrix mass exchange rate coefficients in drying soils at drilosphere scale (Fig. 1) that are still assumed to be constant (Faúndez Urbina et al., 2021; Gerke and Köhne, 2002).

However, such remark must be taken into account when analysing the upscaled hydraulic conductivity of the numerical model (Fig. 1). Fitting the soil water retention using uni- and bimodal retention functions (Durner, 1994) to the volumetric water content and pressure head obtained from the DEM-2PFV approach may be used to quantify the unsaturated hydraulic conductivity at biopore-matrix scale and at drilosphere scale afterwards. Furthermore, the water content distribution obtained from pore scale simulations can be directed to explore a wider range of pressure head, determining shrinkage curves for soils of different physical properties (Peng and Horn, 2005). This would allow expanding investigations of how micro parameters and their heterogeneity affect the different shrinkage phases at drilosphere scale (Schäffer et al., 2013), providing macroscopic measures of soil structural dynamics (Fig. 1) (Bottinelli et al., 2016).

5. Conclusions

By quantifying the macro parameters of stress–strain curve, this study confirmed that the coating material present in biopore surfaces increases the radial hydro-structural stability of soil samples. In addition, the strong correlation of the empirical macro parameters of the primary and secondary stress–strain stages with the pore-scale model micro parameters allows parameterization when using a multi-output regression with random forest *meta*-estimator.

The developed poly-dispersed discrete element model could be coupled with pore finite volume model to describe the interdependent effects of two-phase air–water flow and shrinkage on a structured soil with earthworm burrow coating during drainage. The consistent simulation results reveal the usefulness of the specific novelty of the DEM-2PFV model in form of the aggregation of DEM particles to represent both, the finer-textured porous aggregates of clay-organic coated burrow walls and the coarser-textured porous aggregates of the soil matrix. This model reproduced the effective stress-dependent dynamics of the inter- and intra-aggregate pore networks of both the coating material and the matrix. Consequently, the machine learning model revealed that the bond strength among particles within aggregates governs the shrinkage of soil matrix, while the particle stiffness of the coating material reduces the susceptibility of aggregates breakage by producing a more stable inter-aggregate pore network during drainage.

The pore scale DEM-2PFV model sheds light on soil hydro-mechanical processes, which could help to study the dynamics of macropore – matrix mass exchange through coated earthworm burrow surfaces during preferential flow events and the alteration of soil shrinkage and crack propagation in the coated biopore wall and the surrounding soil matrix. Moreover, the parameterization approach captures the importance of micro scale parameters (i.e., pore-scale level) on macro scale (i.e., pedon or field scale level) measurements. The DEM-2PFV model-based analysis may allow identifying processes and heterogeneities at micro scale and help to properly represent these processes when generating upscaled models. The microscale hydro-mechanic modelling may be useful for finding effective flow exchange parameters in upscaled models and correlating pore-scale parameters to experimentally determined stress–strain macro parameters.

Declaration of Competing Interest

The authors declare that they have no known competing financial interests or personal relationships that could have appeared to influence the work reported in this paper.

Data availability

Data will be made available on request.

Acknowledgments

We gratefully acknowledge the financial support by the German Research Foundation (DFG) under grant GE 990/14-1, entitled: “The exchange flow between preferential flow paths and matrix in soils: from pore to continuum scale with tensors” (FLEXPO). Thanks to Kristian Berger (ZALF) and Annelie Ehrhardt (ZALF) for the technical support in the laboratory.

Appendix A. Supplementary data

Supplementary data to this article can be found online at https://doi.org/10.1016/j.geoderma.2023.116497.

References

Asaf, Z., Rubinstein, D., Shmulevich, I., 2007. Determination of discrete element model parameters required for soil tillage. Soil Tillage Res. 92, 227–242. https://doi.org/10.1016/j.still.2006.03.006.

Badorreck, A., Gerke, H.H., Hüttl, R.F., 2012. Effects of Ground-dwelling beetle burrows on infiltration patterns and pore structure of initial soil surfaces. Vadose Zo. J. 11 https://doi.org/10.2136/vzj2011.0109.

Barbosa, L.A.P., 2020. Modelling the aggregate structure of a bulk soil to quantify fragmentation properties and energy demand of soil tillage tools in the formation of seedbeds. Biosyst. Eng. 197, 203–215. https://doi.org/10.1016/j.biosystemseng.2020.06.019.

Barbosa, L.A.P., Gerke, H.H., 2022. Structural heterogeneity of soil clods: correlating Weibull parameters to fracture surface topography. Geoderma 428, 116161. https://doi.org/10.1016/j.geoderma.2022.116161.

Barbosa, L.A.P., Keller, T., Ferraz, A.C.de.O., 2020. Scale effect of aggregate rupture: using the relationship between friability and fractal dimension to parameterise discrete element models. Powder Technol. 375, 327–336. https://doi.org/10.1016/j.powtec.2020.08.006.

Barbosa, L.A.P., Gerke, K.M., Gerke, H.H., 2022a. Modelling of soil mechanical stability and hydraulic permeability of the interface between coated biopore and matrix pore regions. Geoderma 410, 115673. https://doi.org/10.1016/j.geoderma.2021.115673.

Barbosa, L.A.P., Gerke, K.M., Munkholm, L.J., Keller, T., Gerke, H.H., 2022b. Discrete element modeling of aggregate shape and internal structure effects on Weibull distribution of tensile strength. Soil Tillage Res. 219, 105341 https://doi.org/10.1016/j.still.2022.105341.

Becker, J.N., Holz, M., 2021. Hot or not? connecting rhizosphere hotspots to total soil respiration. Plant Soil 464, 489–499. https://doi.org/10.1007/s11104-021-04963-4.

Bentz, J., Patel, R.A., Benard, P., Lieu, A., Haupenthal, A., Kroener, E., 2022. How Heterogeneous Pore Scale Distributions of Wettability Affect Infiltration into Porous Media 1–25.

Bishop, A., 1960. The principles of effective stress. Oslo.

Boivin, P., Garnier, P., Vauclin, M., 2006. Modeling the soil shrinkage and water retention curves with the same equations. Soil Sci. Soc. Am. J. 70, 1082–1093. https://doi.org/10.2136/sssaj2005.0218.

Bottinelli, N., Zhou, H., Boivin, P., Zhang, Z.B., Jouquet, P., Hartmann, C., Peng, X., 2016. Macropores generated during shrinkage in two paddy soils using X-ray micro-computed tomography. Geoderma 265, 78–86. https://doi.org/10.1016/j.geoderma.2015.11.011.

Braudeau, E., Costantini, J.M., Bellier, G., Colleuille, H., 1999. New device and method for soil shrinkage curve measurement and characterization. Soil Sci. Soc. Am. J. 63, 525–535. https://doi.org/10.2136/sssaj1999.03615995006300030015x.

Bundt, M., Widmer, F., Pesaro, M., Zeyer, J., Blaser, P., 2001. Preferential flow paths: biological 'hot spots' in soils. Soil Biol. Biochem. 33, 729–738. https://doi.org/10.1016/S0038-0717(00)00218-2.

Capowiez, Y., Gilbert, F., Vallat, A., Poggiale, J.C., Bonzom, J.M., 2021. Depth distribution of soil organic matter and burrowing activity of earthworms—mesocosm study using X-ray tomography and luminophores. Biol. Fertil. Soils 57, 337–346. https://doi.org/10.1007/s00374-020-01536-y.

Chareyre, B., Cortis, A., Catalano, E., Barthélemy, E., 2012. Pore-scale modeling of viscous flow and induced forces in dense sphere packings. Transp. Porous Media 94, 595–615. https://doi.org/10.1007/s11242-012-0057-2.

Cil, M.B., Alshibli, K.A., 2012. 3D assessment of fracture of sand particles using discrete element method. Géotechnique Lett. 2, 161–166. https://doi.org/10.1680/geolett.12.00024.

Coetzee, C.J., Els, D.N.J., 2009. Calibration of granular material parameters for DEM modelling and numerical verification by blade–granular material interaction. J. Terramechanics 46, 15–26. https://doi.org/10.1016/j.jterra.2008.12.004.

Cundall, P.A., Strack, O.D.L., 1979. A discrete numerical model for granular assemblies. Geotechnique 29 (1), 47–65.

Czarnes, S., Hallett, P.D., Bengough, A.G., Young, I.M., 2000. Root- and microbial-derived mucilages affect soil structure and water transport. Eur. J. Soil Sci. 51, 435–443. https://doi.org/10.1046/j.1365-2389.2000.00327.x.

Dal Ferro, N., Strozzi, A.G., Duwig, C., Delmas, P., Charrier, P., Morari, F., 2015. Application of smoothed particle hydrodynamics (SPH) and pore morphologic model to predict saturated water conductivity from X-ray CT imaging in a silty loam Cambisol. Geoderma 255–256, 27–34. https://doi.org/10.1016/j.geoderma.2015.04.019.

Durner, W., 1994. Hydraulic conductivity estimation for soils with heterogeneous pore structure. Water Resour. Res. 30, 211–223. https://doi.org/10.1029/93WR02676.

Ellerbrock, R.H., Gerke, H.H., 2013. Characterization of organic matter composition of soil and flow path surfaces based on physicochemical principles-a review, 1st ed, Advances in Agronomy. Copyright © 2013 Elsevier Inc. https://doi.org/10.1016/B978-0-12-407685-3.00003-7.

Faúndez Urbina, C.A., van Dam, J., Tang, D., Gooren, H., Ritsema, C., 2021. Estimating macropore parameters for HYDRUS using a meta-model. Eur. J. Soil Sci. 72, 2006–2019. https://doi.org/10.1111/ejss.13103.

Gerke, H.H., 2006. Preferential flow descriptions for structured soils. J. Plant Nutr. Soil Sci. 169, 382–400. https://doi.org/10.1002/jpln.200521955.

Gerke, H.H., Köhne, J.M., 2002. Estimating hydraulic properties of soil aggregate skins from sorptivity and water retention. Soil Sci. Soc. Am. J. 66, 26–36. https://doi.org/10.2136/sssaj2002.2600.

Gerke, H.H., van Genuchten, M.T., 1996. Macroscopic representation of structural geometry for simulating water and solute movement in dual-porosity media. Adv. Water Resour. 19, 343–357. https://doi.org/10.1016/0309-1708(96)00012-7.

Haas, C., Horn, R., Ellerbrock, R.H., Gerke, H.H., 2020. Fluorescence imaging for mm-scale observation of macropore-matrix mass transfer: calibration experiments. Geoderma 360, 114002. https://doi.org/10.1016/j.geoderma.2019.114002.

Huang, C., Shao, M., Tan, W., 2011. Soil shrinkage and hydrostructural characteristics of three swelling soils in Shaanxi, China. J. Soils Sediments 11, 474–481. https://doi.org/10.1007/s11368-011-0333-8.

Jarvis, N.J., 2007. A review of non-equilibrium water flow and solute transport in soil macropores: principles, controlling factors and consequences for water quality. Eur. J. Soil Sci. 58, 523–546. https://doi.org/10.1111/j.1365-2389.2007.00915.x.

Keller, T., Lamandé, M., Peth, S., Berli, M., Delenne, J.Y., Baumgarten, W., Rabbel, W., Radjaï, F., Rajchenbach, J., Selvadurai, A.P.S., Or, D., 2013. An interdisciplinary approach towards improved understanding of soil deformation during compaction. Soil Tillage Res. 128, 61–80. https://doi.org/10.1016/j.still.2012.10.004.

Klejment, P., 2021. Application of supervised machine learning as a method for identifying DEM contact law parameters. Math. Biosci. Eng. 18, 7490–7505. https://doi.org/10.3934/mbe.2021370.

Köhne, J.M., Köhne, S., Šimůnek, J., 2009. A review of model applications for structured soils: a) Water flow and tracer transport. J. Contam. Hydrol. 104, 4–35. https://doi.org/10.1016/j.jconhyd.2008.10.002.

Köhne, J.M., Schlüter, S., Vogel, H.-J., 2011. Predicting solute transport in structured soil using pore network models. Vadose Zo. J. 10, 1082–1096. https://doi.org/10.2136/vzj2010.0158.

Le Mer, G., Jouquet, P., Capowiez, Y., Maeght, J., Tran, T.M., Doan, T.T., Bottinelli, N., 2021. Age matters: dynamics of earthworm casts and burrows produced by the anecic Amynthas khami and their effects on soil water infiltration. Geoderma 382, 114709. https://doi.org/10.1016/j.geoderma.2020.114709.

Legland, D., Arganda-Carreras, I., Andrey, P., 2016. MorphoLibJ: integrated library and plugins for mathematical morphology with ImageJ. Bioinformatics 32, 3532–3534. https://doi.org/10.1093/bioinformatics/btw413.

Leue, M., Holz, M., Gerke, H.H., Taube, R., Puppe, D., Wirth, S., 2021. Spatially-distributed microbial enzyme activities at intact, coated macropore surfaces in Luvisol Bt-horizons. Soil Biol. Biochem. 156, 108193 https://doi.org/10.1016/j.soilbio.2021.108193.

Lucas, M., Schlüter, S., Vogel, H.J., Vetterlein, D., 2019. Roots compact the surrounding soil depending on the structures they encounter. Sci. Rep. 9, 1–13. https://doi.org/10.1038/s41598-019-52665-w.

McDowell, G.R., Bolton, M.D., 1998. On the micromechanics of crushable aggregates. Géotechnique 48, 667–679. https://doi.org/10.1680/geot.2000.50.3.315.

McDowell, G.R., Bono, J.P.de, 2013. On the micro mechanics of one-dimensional normal compression. Geotechnique 63, 895–908. https://doi.org/10.1680/geot.12.P.041.

Meakin, P., Tartakovsky, A.M., 2009. Modeling and simulation of pore-scale multiphase fluid flow and reactive transport in fractured and porous media. Rev. Geophys. 47, 1–47. https://doi.org/10.1029/2008RG000263.

Morales, V.L., Parlange, J.Y., Steenhuis, T.S., 2010. Are preferential flow paths perpetuated by microbial activity in the soil matrix? A review. J. Hydrol. 393, 29–36. https://doi.org/10.1016/j.jhydrol.2009.12.048.

Morrissey, J.W., Rice, J.R., 1998. Crack front waves. J. Mech. Phys. Solids 46, 467–487. https://doi.org/10.1016/S0022-5096(97)00072-0.

Mueller, S.B., Kueppers, U., Ametsbichler, J., Cimarelli, C., Merrison, J.P., Poret, M., Wadsworth, F.B., Dingwell, D.B., 2017. Stability of volcanic ash aggregates and break-up processes. Sci. Rep. 7 https://doi.org/10.1038/s41598-017-07927-w.

Niya, S.M.R., Selvadurai, A.P.S., 2018. A statistical correlation between permeability, porosity, tortuosity and conductance. Transp. Porous Media 121, 741–752. https://doi.org/10.1007/s11242-017-0983-0.

Pedregosa, F., Varoquaux, G., Gramfort, A., Michel, V., Thirion, B., Grisel, O., Blondel, M., Prettenhofer, P., Weiss, R., Dubourg, V., Vanderplas, J., Passos, A., Cournapeau, D., Brucher, M., Perrot, M., Douchesnay, É., 2011. Scikit-learn: machine learning in Python Fabian. J. Machine Learn. Res. 12, 2825–2830.

Peng, X., Hallett, P.D., Zhang, B., Horn, R., 2011. Physical response of rigid and non-rigid soils to analogues of biological exudates. Eur. J. Soil Sci. 62, 676–684. https://doi.org/10.1111/j.1365-2389.2011.01383.x.

Peng, X., Horn, R., 2005. Modeling soil shrinkage curve across a wide range of soil types. Soil Sci. Soc. Am. J. 69, 584–592. https://doi.org/10.2136/sssaj2004.0146.

Pion, S., Teillaud, M., 2011. 3D triangulations, in: CGAL User and Reference Manual. CGAL Editorial Board.

Rieckh, H., Gerke, H.H., Sommer, M., 2012. Hydraulic properties of characteristic horizons depending on relief position and structure in a hummocky glacial soil landscape. Soil Tillage Res. 125, 123–131. https://doi.org/10.1016/j.still.2012.07.004.

Ruiz, S., Or, D., Schymanski, S.J., Balestrini, R., 2015. Soil penetration by earthworms and plant roots - Mechanical energetics of bioturbation of compacted soils. PLoS One 10 (6), e0128914.

Schäffer, B., Mueller, T.L., Stauber, M., Müller, R., Keller, M., Schulin, R., 2008a. Soil and macro-pores under uniaxial compression. II. Morphometric analysis of macro-pore stability in undisturbed and repacked soil. Geoderma 146, 175–182. https://doi.org/10.1016/j.geoderma.2008.05.020.

Schäffer, B., Stauber, M., Mueller, T.L., Müller, R., Schulin, R., 2008b. Soil and macro-pores under uniaxial compression. I. Mechanical stability of repacked soil and deformation of different types of macro-pores. Geoderma 146, 183–191. https://doi.org/10.1016/j.geoderma.2008.05.019.

Schäffer, B., Schulin, R., Boivin, P., 2013. Shrinkage properties of repacked soil at different states of uniaxial compression. Soil Sci. Soc. Am. J. 77, 1930–1943. https://doi.org/10.2136/sssaj2013.01.0035.

Schindelin, J., Arganda-Carreras, I., Frise, E., Kaynig, V., Longair, M., Pietzsch, T., Preibisch, S., Rueden, C., Saalfeld, S., Schmid, B., Tinevez, J.-Y., White, D.J., Hartenstein, V., Eliceiri, K., Tomancak, P., Cardona, A., 2012. Fiji: an open-source platform for biological-image analysis. Nat. Methods 9, 676–682. https://doi.org/10.1038/nmeth.2019.

Scholtès, L., Donzé, F.-V., 2012. A DEM model for soft and hard rocks: role of grain interlocking on strength. J. Mech. Phys. Solids 61, 352–369. https://doi.org/10.1016/j.jmps.2012.10.005.

Scholtès, L., Donzé, F.V., 2015. A DEM analysis of step-path failure in jointed rock slopes. Comptes Rendus Mécanique 343, 155–165. https://doi.org/10.1016/j.crme.2014.11.002.

Shipitalo, M.J., Dick, W.A., Edwards, W.M., 2000. Conservation tillage and macropore factors that affect water movement and the fate of chemicals. Soil Tillage Res. 53, 167–183. https://doi.org/10.1016/S0167-1987(99)00104-X.

Šmilauer, V., Chareyre, B., Duriez, J., Eulitz, A., Gladky, A., Guo, N., Jakob, C., Kozicki, J., 2015. Using and programming. Yade Doc. 2 https://doi.org/10.5281/zenodo.34043.

Tang, C.S., Zhu, C., Cheng, Q., Zeng, H., Xu, J.J., Tian, B.G., Shi, B., 2021. Desiccation cracking of soils: a review of investigation approaches, underlying mechanisms, and influencing factors. Earth-Sci. Rev. 216, 103586 https://doi.org/10.1016/j.earscirev.2021.103586.

van der Linden, J.H., Tordesillas, A., Narsilio, G.A., 2019. Preferential flow pathways in a deforming granular material: self-organization into functional groups for optimized global transport. Sci. Rep. 9, 1–15. https://doi.org/10.1038/s41598-019-54699-6.

Vereecken, H., Schnepf, A., Hopmans, J.W., Javaux, M., Or, D., Roose, T., Vanderborght, J., Young, M.H., Amelung, W., Aitkenhead, M., Allison, S.D., Assouline, S., Baveye, P., Berli, M., Brüggemann, N., Finke, P., Flury, M., Gaiser, T., Govers, G., Ghezzehei, T., Hallett, P., Hendricks Franssen, H.J., Heppell, J., Horn, R., Huisman, J.A., Jacques, D., Jonard, F., Kollet, S., Lafolie, F., Lamorski, K., Leitner, D., McBratney, A., Minasny, B., Montzka, C., Nowak, W., Pachepsky, Y., Padarian, J., Romano, N., Roth, K., Rothfuss, Y., Rowe, E.C., Schwen, A., Šimůnek, J., Tiktak, A., Van Dam, J., van der Zee, S.E.A.T.M., Vogel, H.J., Vrugt, J.A., Wöhling, T., Young, I.M., 2016. Modeling soil processes: review, key challenges, and new perspectives. Vadose Zo. J. 15 (5) https://doi.org/10.2136/vzj2015.09.0131.

Vogel, H.J., Balseiro-Romero, M., Kravchenko, A., Otten, W., Pot, V., Schlüter, S., Weller, U., Baveye, P.C., 2022. A holistic perspective on soil architecture is needed as a key to soil functions. Eur. J. Soil Sci. 73, 1–14. https://doi.org/10.1111/ejss.13152.

Wu, Y., Yamamoto, H., Izumi, A., 2016. Experimental investigation on crushing of granular material in one-dimensional test. Period. Polytech. Civ. Eng. 60, 27–36. https://doi.org/10.3311/PPci.8028.

Yuan, C., Chareyre, B., 2017. A pore-scale method for hydromechanical coupling in deformable granular media. Comput. Methods Appl. Mech. Eng. 318, 1066–1079. https://doi.org/10.1016/j.cma.2017.02.024.

Yuan, C., Chareyre, B., 2021. Transitioning from the funicular to the pendular regime in granular soils. Géotechnique 72 (9), 825–831.

Yuan, C., Chareyre, B., Darve, F., 2016. Pore-scale simulations of drainage in granular materials: finite size effects and the representative elementary volume. Adv. Water Resour. 95, 109–124. https://doi.org/10.1016/j.advwatres.2015.11.018.